Validation and Benchmark Cases

13.1. Introduction

Since even the most carefully conceived and constructed model is subject to coding errors, there is an ever-present need for validation tests to verify the integrity of all or part of a computer code. The nature of these tests can vary from simply checking the symmetry of flows which should remain symmetric to testing the invariance of certain integral quantities (*e.g.*, total energy) to comparing model results with known exact solutions of the Navier-Stokes equations, the equations of motion of a viscous fluid. The exact solutions are particularly relevant to model validation since they provide a means to simultaneously check the integrity of the advection, pressure and frictional calculations as well as the time-stepping procedure. Where exact solutions are not available, it is useful to compare the model solution against solutions obtained from other models.

13.2. Symmetry Tests with Random Initial Perturbations

The indexing error is probably the most common type of coding error in multi-dimensional numerical models. Checking the symmetry (to the degree of machine accuracy) of the model solutions is a seemingly trivial but very valuable test that will, in most cases, uncover this type of error. Many other types of errors can also be revealed by this procedure. Throughout the development cycles of ARPS, symmetry was the first property to be checked. Clark (1979) used a procedure to test individual subroutines for symmetry using successively rotated random fields, and found the practice extremely helpful.

In ARPS, the option to initialize potential temperature perturbations with a build-in symmetric random number generator is available. These random numbers are determined once and for all once the grid setup

parameters are given. If the initial perturbations, the base state and the model grid are all symmetric, the model solution should, in the absence of the Coriolis force and base-state horizontal winds, remain symmetric. Symmetry can be checked by looking at the maximum and minimum values of the horizontal velocity fields; they should be either symmetric or anti-symmetric about the central axis of the grid. ARPS also has debug printing options to facilitate the examination of the model solution. These options print the left to right or front to back difference fields. If these fields are symmetric these printed difference fields should be exactly zero or on the order of the machine round-off error.

These symmetry tests check as many of the subroutines as possible, for example, terrain, grid stretching, vertically explicit and implicit solvers, turbulence, computational mixing, divergence damping, microphysics, open boundary conditions, surface physics and the soil model. However, we must turn off the Coriolis force and the dependency of the surface heat on the solar angle in the surface energy budget equation. Mutually exclusive options such as the warm rain and ice microphysics have to be tested separately.

As part of a standard validation test suite, a set of symmetry experiments was designed. The common parameters of these experiments are listed as follows:

The dimensions are $nx = ny = 19$, $nz = 20$. $\Delta x = \Delta y = 1000$ m. The vertical grid stretching option 2 is used with $\Delta z_{min} = 200$ m and an average $\Delta z = 500$ m. A 1 km height bell-shaped mountain with a half-width of 5 km is located at the center of the domain (8 km). The symmetric random perturbation has an initial amplitude of 4 K. The sounding file *may20_calm.snd* is used. The model center is at (-100°, 35°) longitude-latitude. The big time step size is 6 s and the small time step size is 1 s. The warm rain and ice microphysics options are tested separately. The surface physics option is set to 4 (stability dependent surface fluxes from the soil-model predicted surface variables). The dependency of the solar angle to the grid location is turned off. The Coriolis force is turned off. The Smagorinsky and TKE turbulence parameterizations are tested separately. Both 2nd and 4th order computational mixings are switched on, with both coefficients equal to 5×10^{-4}. The Rayleigh damping layer starts at $z = 6$ km, and the damping coefficient is 0.01 s^{-1}. The coefficient of the Asselin time filter is 0.10.

Parameters / model configurations specific for individual experiments are as follows:

RSYM1: 3-D, Vertically explicit solver, Klemp and Wilhelmson (*rbcopt* = 1) open boundary condition with phase speed of 300 m/s. Warm rain microphysics. Smagorinsky turbulence;

RSYM2: as RSYM1, but in 2-D *x*-*z* mode, *ny* = 4, periodic south and north boundary conditions;

RSYM3: as RSYM1, but in 2-D *y-z* mode, *nx* = 4, periodic east and west boundary conditions;
RSYM4: as RSYM1, but using vertically implicit solver;
RSYM5: as RSYM1, but using 1.5 order TKE turbulence;
RSYM6: as RSYM1, but using ice microphysics

The above experiments were conducted on the Cray YMP, which has a default 64 bit word length corresponding to double precision on 32 bit machines. The maximum and minimum diagnostics were printed every large time step, and found that the symmetry was maintained up to the 10th digit after the decimal point in the maximum and minimum velocity values. On the 32 bit machine, the symmetry is usually maintained up to the 6th digit after the decimal place.

If an asymmetry occurs, an effective procedure to isolate the cause of the asymmetry is to turn off as many of the options as possible, and run the model in a simple 2-D configuration. First make sure the solution is symmetric for this simplest of cases and then add options, one by one, until the asymmetry appears. This will provide clues to the most probable source of the problem.

13.3. A Viscous Beltrami Flow Test

Despite the fundamental role of the Navier-Stokes equations in the study of atmospheric, oceanographic and engineering problems, few exact solutions have been obtained. The difficulty in solving the Navier-Stokes equations analytically stems from the presence of non-linear terms associated with fluid inertia which render conventional (*i.e.*, linear) analysis techniques powerless in the general case. Exact solutions have been obtained only in special cases for which the non-linearity could be cast in a tractable form or tricked into falling out of the analysis. Moreover, among these rare flows, only those which are free of singularities are suitable for validation tests. Candidates for model validation can be grouped as: (i) flows for which the non-linear terms vanish identically for all space and time and (ii) flows for which the non-linear terms taken as a sum (but not individually) vanish identically in the vorticity equation derived from the Navier-Stokes equations. Flows in the former class include steady and unsteady Poiseuille and Couette flows in a variety of flow geometries, oscillatory or impulsive motion of a flat plate moving in its own plane and Ekman flows (*cf.* Batchelor, 1967). Flows in the latter class include viscous Beltrami ($\vec{v} \times \vec{\omega} \equiv 0$) and generalized Beltrami flows ($\nabla \times \vec{v} \times \vec{\omega} \equiv 0$), where $\vec{v}$ is the velocity vector and $\vec{\omega}$ the vorticity vector. Taylor's two-dimensional decaying vortex grid (Rosenhead 1963) is perhaps the best known generalized Beltrami flow.

In this section we describe a validation test of the ARPS code with a three-dimensional constant-viscosity Beltrami solution of the (incompressible) Navier-Stokes equations. A complete account of this test can be found in Shapiro (1993). The solution is a viscously decaying Beltrami flow characterized by counter-rotating updrafts and downdrafts and represents a simple extension of a steady, inviscid flow outlined by Lilly (1983, 1986) in studies of thunderstorm rotation. The solution to this flow is

$$u = -\frac{A}{k^2 + l^2}\left[\lambda l \cos(kx)\sin(ly)\sin(mz) + mk\sin(kx)\cos(ly)\cos(mz)\right]\exp\left(-\nu\lambda^2 t\right)$$

$$v = \frac{A}{k^2 + l^2}\left[\lambda k \sin(kx)\cos(ly)\sin(mz) - ml\cos(kx)\sin(ly)\cos(mz)\right]\exp\left(-\nu\lambda^2 t\right)$$

$$w = A\cos(kx)\cos(ly)\sin(mz)\exp\left(-\nu\lambda^2 t\right)$$

$$p = p_S - \rho\left(\frac{u^2 + v^2 + w^2}{2} + gz\right)$$

where

$$\lambda^2 = k^2 + l^2 + m^2,$$

p is the perturbation pressure, p_S is the stagnation pressure at ground level, A is the amplitude of the vertical velocity and u, v and w are the x, y and z components of the velocity vector, respectively.

For our test we take one full wave in the y and z directions and two full waves in the x direction: $k = 4\pi/L_x$, $l = 2\pi/L_y$ and $m = 2\pi/L_z$, where the physical dimensions of the domain are $L_x = 267$ m, $L_y = 118$ m, and $L_z = 44$ m. The height of the flow domain was chosen to be much smaller than the density scale height to avoid potential discrepancies between the full compressible model solution and the exact incompressible solution. The grid spacings are $dx = 3$ m, $dy = 2$ m, and $dz = 1$ m. The number of computational grid points (physical grid points + 2) is $nx = 92$, $ny = 62$ and $nz = 47$. Periodic boundary conditions were imposed on both lateral and vertical boundaries.

The amplitude of the vertical velocity is A = 2 m s^{-1} and the fluid is characterized by a (constant) kinematic viscosity of ν = 1 m^2 s^{-1} and a (constant) base state potential temperature of 300 K.

The model is integrated for over two e-folding decay time periods. Given our choice of input parameters the decay time of the exact solution, $T = 1/(\nu\lambda^2)$, is approximately 40 seconds. Based on CFL stability criteria we estimated a conservative large time step as 0.19 s and a conservative small time step as 0.002 s.

Figure 13.1 depicts the model-predicted and exact horizontal velocity fields on a selected horizontal cross section at 41 s. Very good agreement is apparent between the numerical and the exact solutions on this cross section, with a maximum relative error on the order of 3 %. Other horizontal and vertical cross sections examined at 41 s and 82 s (not shown) revealed comparable agreement between ARPS-predicted velocity field and the theoretical solution. The time evolution of the domain-maximum predicted winds and the theoretical wind maxima presented in Figure 13.2 also suggest a good agreement between the numerical and exact solutions. In view of these test results, the integrity of the dynamical portion of the ARPS code is amply verified, at least for the constant eddy viscosity and periodic boundary condition options.

Other tests were performed, for example, by reducing the eddy viscosity by 50 % while turning on a second order computational mixing term to make up the difference and by turning on a divergence damper to reduce the amplitude of the sound waves. In all cases the u, v and w results were indistinguishable from those in the original test case.

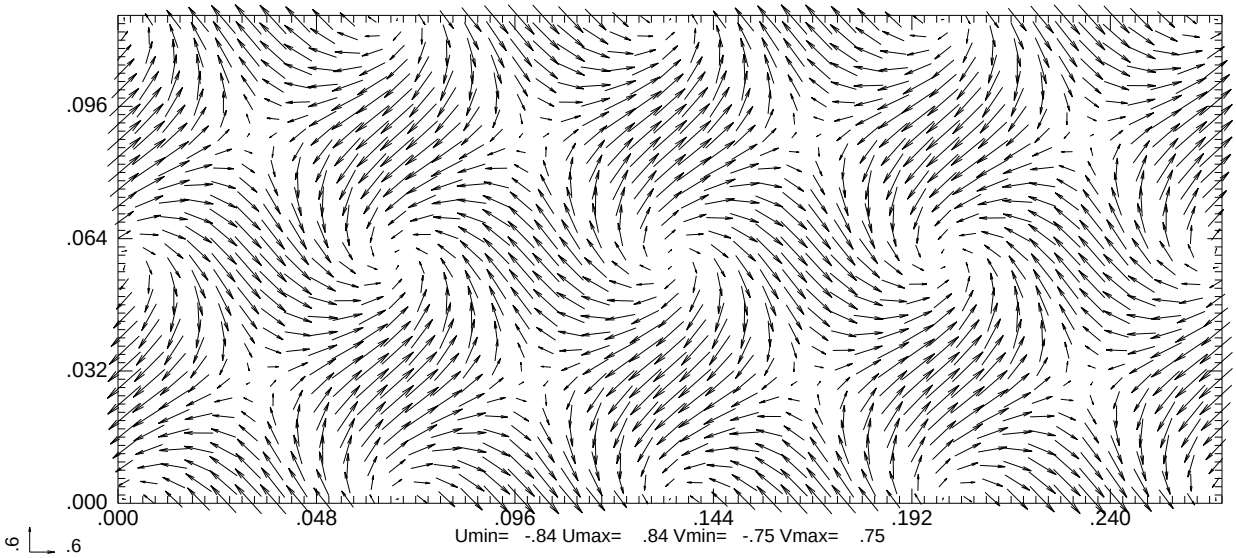

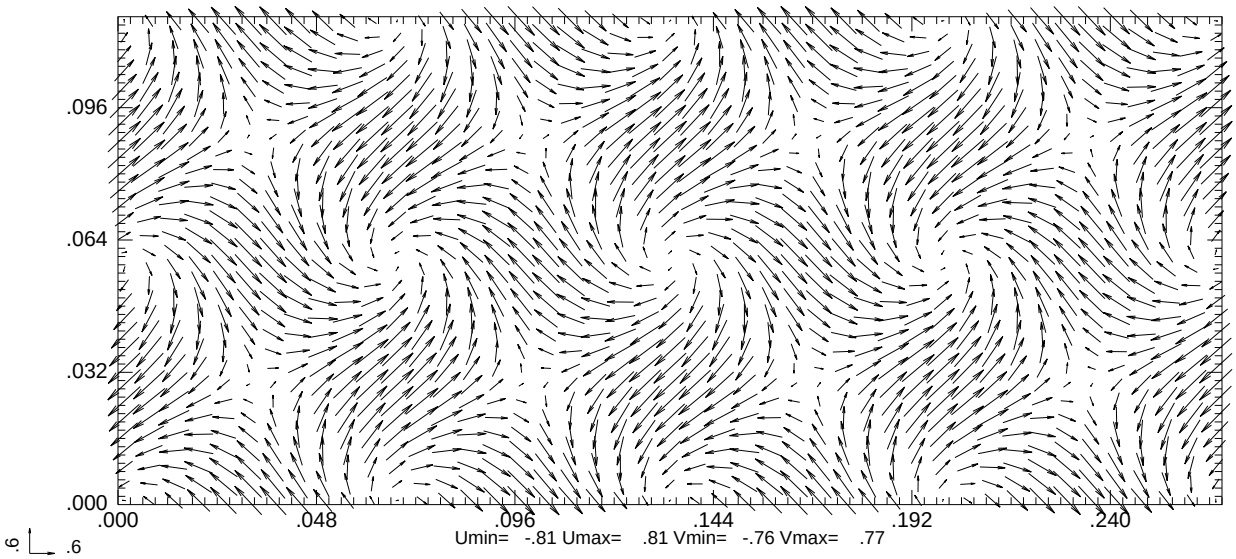

b)

Figure 13.1 Horizontal velocity vector fields for the ARPS validation test at t = 41 s (216 large time steps) on k = 7. (a) Exact solution. (b) ARPS predicted solution. Velocity vectors are presented for every other grid point. The solution has the same pattern as in the initial condition but has decayed in time by a factor of just over e^{-1}.

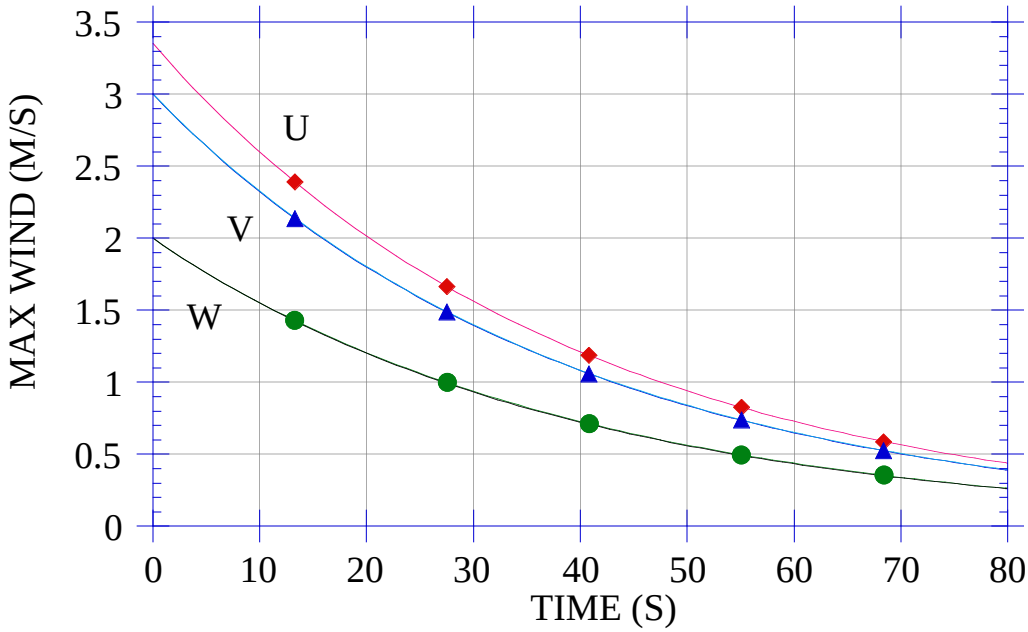

Figure 13.2. Evolution of domain-maximum u, v and w for the ARPS validation test. The model is run for just over two e-folding decay times (~ 82 s). ARPS solution is indicated by solid symbols, the exact solution by solid lines.

13.4. A Test of the Coriolis Formulation

Provision is made in ARPS for a complete specification of the Coriolis force, including terms in both the vertical and horizontal equations of motion. The user is provided with options for either turning off the Coriolis force, turning on a "conventional" Coriolis force (*i.e.*, terms involving $f = 2\Omega \sin\phi$), or turning on the complete Coriolis formulation. We now examine a test of the complete Coriolis formulation.

In the complete formulation of the Coriolis force on an f-plane, extra terms in the equations of motion appear as (*cf.* Holton, 1979):

$$\frac{\partial \bar{\rho} u}{\partial t} = ... \; 2\Omega \sin\phi \, \bar{\rho} v \; - \; 2\Omega \cos\phi \, \bar{\rho} w$$

$$\frac{\partial \bar{\rho} v}{\partial t} = ... - 2\Omega \sin\phi \, \bar{\rho} u$$

$$\frac{\partial \bar{\rho} w}{\partial t} = ... \; 2\Omega \cos\phi \, \bar{\rho} u$$

where $\Omega = 7.292 \times 10^{-5}$ s^{-1} is the earth's angular velocity and ϕ is the latitude.

If the flow is isentropic, the density constant, the initial velocity vector unidirectional and the initial pressure perturbation zero (no deviation from a hydrostatic base state), then all spatial derivatives are initially zero and we can seek solutions of the governing equations for which spatial derivatives are zero for all time (*i.e.*, the Navier-Stokes equations reduce to a set of ordinary differential equations). In this case the velocity field is determined as:

$$u = A\, cos(2\Omega t) + B\, sin(2\Omega t)$$

$$v = -A \sin\phi \sin(2\Omega t) + B sin\phi \cos(2\Omega t) + C$$

$$w = A \cos\phi \sin(2\Omega t) - B cos\phi \cos(2\Omega t) + D$$

where the constants of integration, A, B, C and D, are related to the initial values of the velocity field $u(0) = U$, $v(0) = V$ and $w(0) = W$ by:

$$A = U$$

$$B = \sin\phi \, V - \cos\phi \, W$$

$$C = \cos\phi \left(\cos\phi \, V + \sin\phi \, W \right)$$

$$D = \sin\phi \left(\cos\phi \, V + \sin\phi \, W \right)$$

For the validation test, a grid spacing of dx = 60 m, dy = 30 m, and dz = 15 m with nx = 6, ny = 7, and nz = 5 is imposed. We take U = 2 m s^{-1}, V = 3 m/s and W = 1 m s^{-1}. The latitude, ϕ, is set to 45˚ and Ω is 7.292 × 10^{-5} s^{-1}. The base state potential temperature is set at 300 K and an (irrelevant) eddy viscosity of 10 m^2 s^{-1} is imposed.

The model is integrated for 6 hours, or approximately half an inertial time period. Based on CFL stability criteria, a conservative large time step is estimated as 3.0 s and a conservative small time step as 0.03 s.

Because of the uniform *w* field in this experiment and long time integration, compressibility effects caused substantial deviation from the exact solution derived for an incompressible flow. Since the purpose of the experiment was to test the Coriolis formulation, we considered it legitimate to "short circuit" the model's compressibility by setting the model's base state density equal to a constant and removing the pressure advection term.

The results of the validation test run (without the effects of compressibility) are depicted in Figure 13.3. No spatial gradients appeared in *u*, *v* or *w*. The model predicted solutions for *u*, *v* and *w* agree to within 0.001 m s^{-1} of the analytic solution.

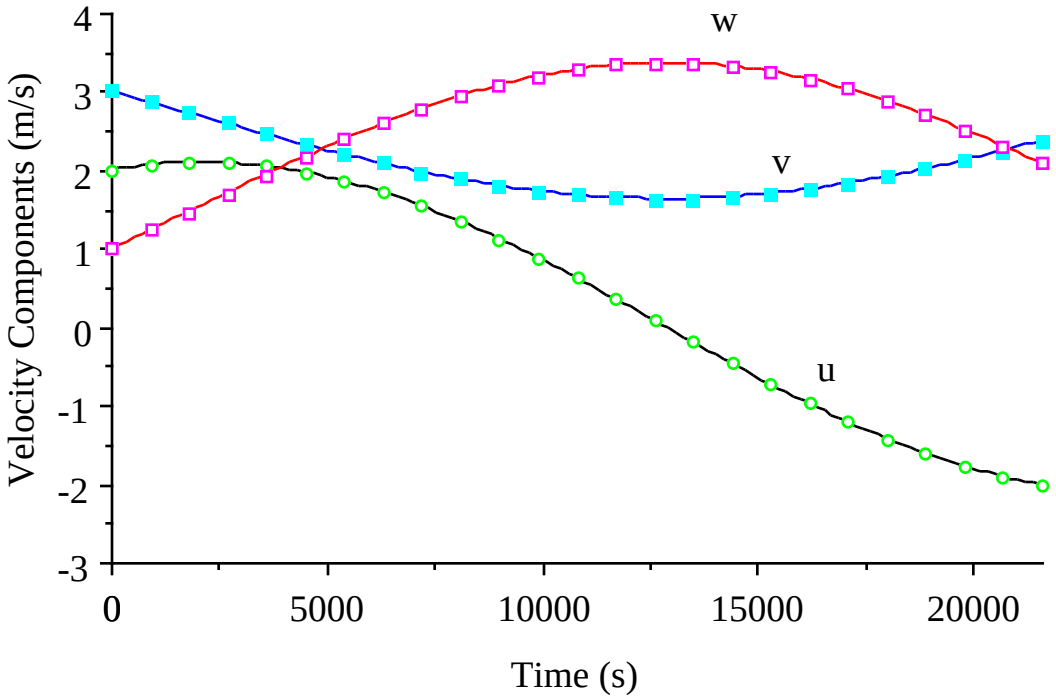

Figure 13.3 A comparison of ARPS *u*, *v* and *w* solution (symbols) with the analytic solution (solid lines) for the rotation of a unidirectional velocity vector by the Coriolis force. The model was run for 6 hours, or approximately half the inertial period.

13.5. A Test with the Taylor-Green Solution

The Taylor-Green solution (Taylor and Green, 1937) describes the "grinding down" of large eddies (vortices) into smaller eddies by nonlinear

processes, that is, the energy cascade from large to small scales. It is not a closed form solution but represents the first few terms of a series expansion (about $t = 0$) of a flow which initially has wavenumbers a, b and c:

$$u = A \cos(ax) \sin(by) \sin(cz)$$

$$v = B \sin(ax) \cos(by) \sin(cz)$$

$$w = C \sin(ax) \sin(by) \cos(cz)$$

where $Aa + Bb + Cc = 0$ for incompressibility. In the subsequent flow these eddies decay and smaller eddies are produced. This solution should not be confused with "Taylor's vortex" (Rosenhead, 1963) which is two-dimensional and hence free of the vortex stretching/tilting mechanism.

The Taylor-Green solution was simulated in an ARPS validation test and compared with the solutions presented in Moeng (1984), *viz.*, the analytic solution (valid only for a short time after $t = 0$), the solution in an alias-free Galerkin model and the solution obtained in a mixed pseudo-spectral finite difference model. The results indicate that ARPS simulates an energy transfer process similar to that in an alias-free spectral model, and higher resolution produces better results. Identical results were obtained by rotating the horizontal axes by 90°, indicating ARPS is free of symmetry error.

13.6. May 20, 1977 Del City Supercell Storm

The 20 May 1977 Del City, Oklahoma storm is a well documented and extensively studied tornadic supercell storm case. For details on the morphology and evolution of this storm, the reader is referred to Ray *et al.* (1981), Klemp *et al.*, (1981) and Klemp and Rotunno (1983).

The ARPS source code provided to users includes the 20 May 1977 Del City sounding file *may20.snd* as well as an input file set up for a two hour storm simulation. The results of this simulation are now presented.

The model grid size is 67x67× 35. The grid interval is 1.0 km in the horizontal and 500 m (uniform) in the vertical. The physical domain size is therefore $64 \times 64 \times 16$ km (subtract 3 from the number of grid points in each direction and multiply the result by the grid spacing). For the purpose of model validation, we present the solution only at one time -- one hour into the integration. The storm was initiated by an isolated thermal bubble described in Chapter 4. The bubble was centered at $x = 48$ km, $y = 16$ km and $z = 1.5$ km, with the origin at the lower front left corner of the grid. The radius of the

bubble was 10 km in both *x* and *y* directions and 1.5 km in the vertical direction. The magnitude of the thermal perturbation was 4 degrees. The TKE subgrid scale turbulence option (*tmixopt* = 4) was used with the turbulent Prandtl number equall to 1 and *kmlimt* = 0.5. for computational mixing. Fourth-order horizontal and second order vertical computational mixing was turned on with *cfcm4h* = 1×10^{-3} s^{-1} and *cfcm2v* = 4×10^{-4} s^{-1}. Rayleigh damping was applied in a layer from 12 km up to the top of the grid and the Rayleigh damping coefficient was 0.0033 s^{-1}. Divergence damping was also switched on with a coefficient of 0.05. The vertical implicit solver was used for *w* and *p* equations, with *tacoef* = 0.6. Surface physics and the Coriolis force were turned off. Orlanski-type radiation boundary conditions with vertically averged phase speed (*rbcopt* = 4) were used, together with boundary relaxation (*rlxlbc* = 0.5) and pressure detrending (*pdetrnd* = 1). Fourth-order horizontal advection (*madvopt* = *sadvopt* = 4) was used for both momentum and scalars. Rigid free-slip conditions were applied to the top and bottom boundaries. The large time step size (*dtbig*) was 6 s and small time step size (*dtsml*) was 1 s. The model was run using Kessler warm rain microphysics.

Time series of the maximum and minimum vertical velocity, *w*, during the two hour time integration are shown in Figure 13.4. It can be seen that the maximum vertical updraft first reached a peak of 38 m s^{-1} at about 60 minutes, then decreased to less than 30 m/s after the storm splits and finally reached 43 m/s at the end of 2 hour simulation.

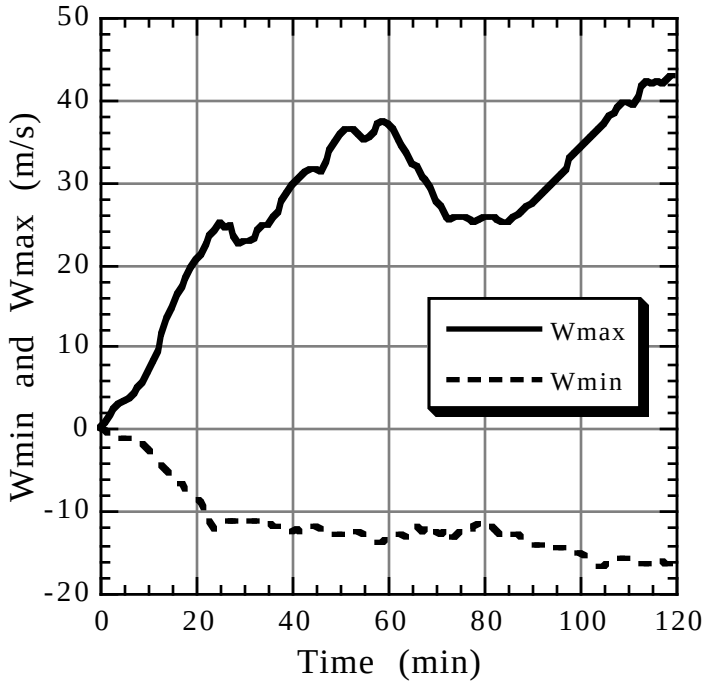

Figure 13.4. The time series of the maximum and minimum vertical velocity in the model domain. W_{max} and W_{min} indicate the maximum strength of the storm updraft and downdraft.

Figure 13.5 shows the fields of horizontal wind, perturbation potential temperature, θ' (dashed lines), and vertical velocity, w (full lines), fields at 250 meters above ground (upper panel) and the fields of horizontal wind and w at the 4 km level (lower panel). It can be seen that by 60 min, storm splitting had occurred. Two distinct updraft centers can be seen at the mid-level, with apparent cyclonic and anti-cyclonic rotation in the horizontal flows around each draft. Underneath the right mover, surface convergence is strong, and the low-level downdraft is mainly associated with the rear-flank gust front. The cold pool induced by rain-water evaporative cooling is clearly shown by the negative temperature contours. These features and their development are consistent with the aforementioned observations and simulation results.

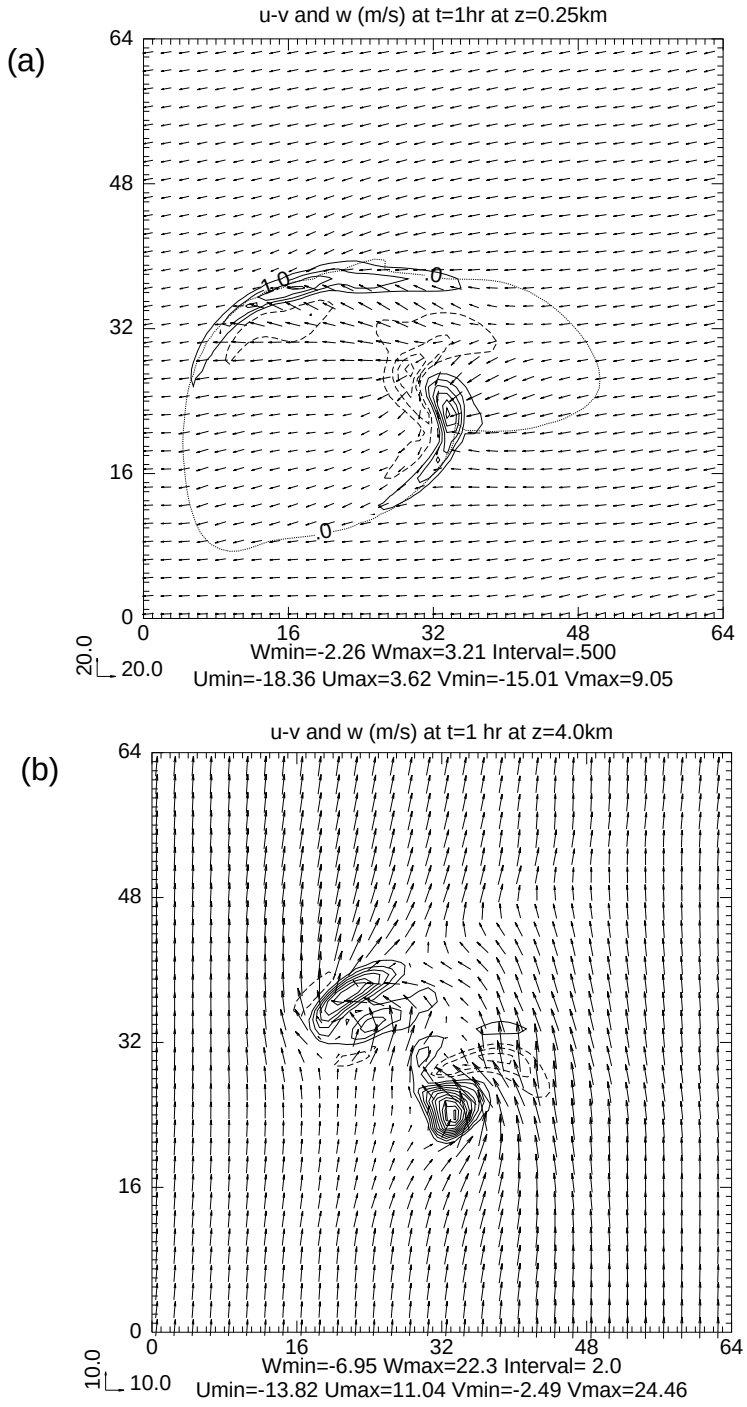

Figure 13.5. Horizontal cross-sections of the model fields of the 20 May 1977 storm simulation at 1 h. a) The horizontal wind vector, perturbation potential temperature, θ', and vertical velocity, w, at z = 250 m. The w contours are in solid (positive) and dashed (negative) lines with a 0.5 m/s contour interval. The θ' contours are in dashed lines with a contour interval of 1 K. b) The horizontal wind vector and w at z = 4 km. The contour interval is 2 m/s.

13.7. Inertia-Gravity Waves in a Constant Flow

The stability and accuracy of the mode-splitting time integration of ARPS was tested with a procedure described in Skamarock and Klemp (1994). In these tests, small amplitude (linear) inertia-gravity waves were simulated in a 2-D periodic channel of length L, with rigid free-slip upper and lower boundaries at $z = 0$ and $z = H$. The waves were excited by an initial potential temperature perturbation of the form:

$$\theta(x,z,0) = \Delta\theta_0 \frac{\sin(\pi z / H)}{1 + (x - x_c)^2 / a^2} \tag{13.7.1}$$

where $\Delta\theta_0$ is a small amplitude (10^{-2} K) potential temperature perturbation and a characterizes the horizontal scale of the perturbation. The Brunt-Väisälä frequency was constant with $N = 10^{-2}$ s^{-1}, and the mean flow speed was U = 20 m/s. With Boussinesq, linear and incompressible approximations, the analytic solution of the ensuing gravity wave motion can be written as (Skamarock and Klemp, 1994):

$$\theta(\tilde{x},z,t) = \theta(\tilde{x},z,0) + \Delta\theta_0 a \sin(lz) \times \int_0^{\infty} \frac{k^2N^2}{k^2N^2 + l^2f^2} \exp(-ak)(\cos\lambda t - 1)\cos(k\tilde{x})dk \tag{13.7.2}$$

where $l = \pi / H$, and $\tilde{x} = x - Ut$ is the x-spatial coordinate moving with the mean advection velocity U, and

$$\lambda^2 = \frac{k^2N^2 + l^2f^2}{k^2 + l^2} . \tag{13.7.3}$$

For our first test case, experiment "sk01a", we took L = 300 km, H = 10 km, a = 5 km, $\Delta x = \Delta z$ = 1 km and integrated to 3000 s. The large time step (*dtbig*) was 12 s and the small time step (*dtsml*) was 3 s. A vertically implicit option (vimplct=1) was chosen for solution of the w and p equations. Periodic boundary conditions were applied on lateral boundaries. Results of this test for the perturbation potential temperature field at 3000 s are displayed in Fig. 13.6(a). For comparison, the analytic solution for the perturbation potential temperature at this time is reproduced in Fig. 13.6(b). Overall, there is good agreement between the ARPS solution and the analytic solution. The numerical solution is slightly distorted in the vertical compared with the analytic solution but this might be expected since the ARPS equations use the

full height-dependent density field whereas the analytic solution is valid to the Boussinesq approximation.

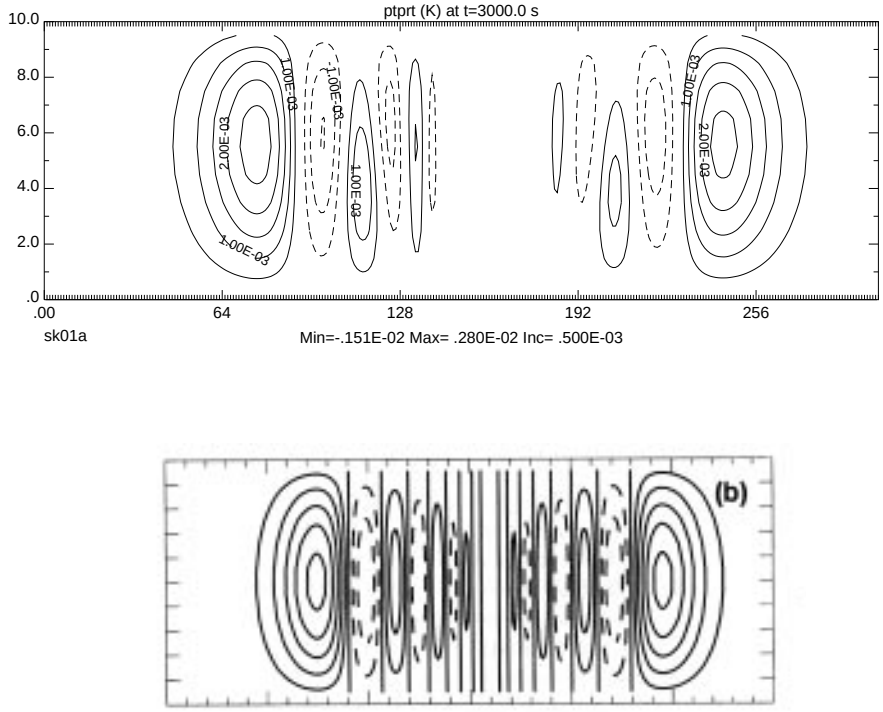

Figure 13.6. Vertical cross-section of potential temperature perturbation at 3000 s for the nonhydrostatic inertia-gravity wave test, experiment sk01a. (a) ARPS-predicted field, (b) analytic solution. Contour increment is 0.5 x 10-3 K. Solid lines represent positive perturbations; dashed lines represent negative perturbations. Figure (b) is part of Fig. 1 of Skamarock and Klemp (1994), reproduced with permission of the American Meteorological Society.

For our next test, experiment "sk01d", we worked with a much wider disturbance: L = 6000 km, H = 10 km, a = 100 km, Δx =20 km and Δz = 1 km, and integrated to 60000 s. The flow in this case should be nearly hydrostatic. The large time step (*dtbig*) was 600 s and the small time step (*dtsml*) was 40 s. The Coriolis force was turned on (*coriopt=1*) at a latitude of 35°. Again, the vertically implicit option (vimplct=1) was chosen for the solution of the w and p equations. In addition, the potential temperature equation was integrated on the small time steps (*ptsmlstp*=1). Periodic boundary conditions were applied

on lateral boundaries. Results of this test for the perturbation potential temperature field at 60000 s are displayed in Fig. 13.7(a). For a comparison, the analytic solution for the perturbation potential temperature at this time is reproduced in Fig. 13.7(b). Again, a reasonable agreement is evident between the ARPS solution and the analytic solution.

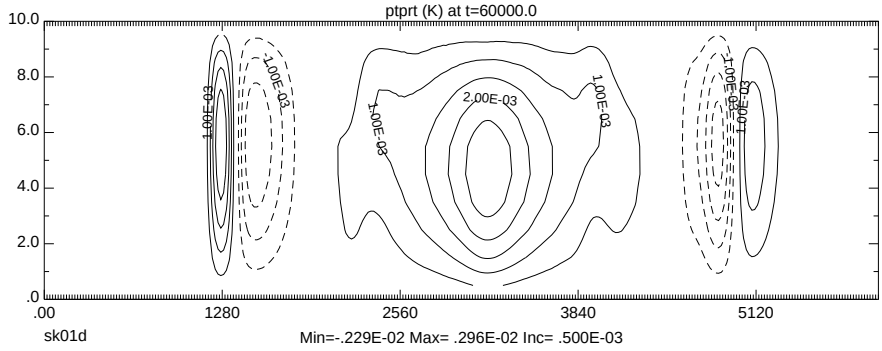

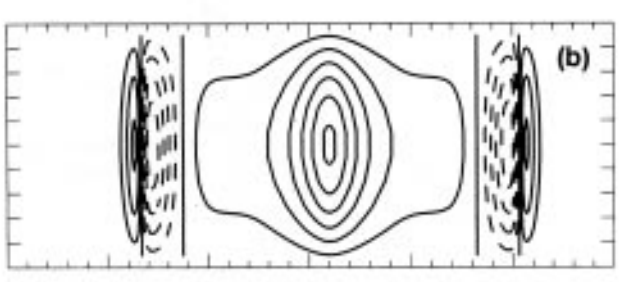

Figure 13.7. Vertical cross-section of potential temperature perturbation at 60000 s for the hydrostatic inertia-gravity wave test, experiment sk01d. (a) ARPS-predicted field, (b) analytic solution. Contour increment is 0.5 x 10-3 K. Solid lines represent positive perturbations; dashed lines represent negative perturbations. Figure (b) is Fig. 3(b) of Skamarock and Klemp (1994), reproduced with permission of the American Meteorological Society.

13.8. Mountain Wave Validation Experiments

13.8.1. Linear Mountain Waves

a) Analytic Solution

The governing equation describing the linearly-forced hydrostatic non-rotational mountain waves in a 2-D anelastic flow can be expressed in terms of perturbation streamlines (see *e.g.*, Smith, 1979)

$$\frac{\partial^2 \delta}{\partial z^2} + l^2 \delta = 0 , \tag{13.8.1}$$

where δ is the displacement streamline and l the Scorer parameter. For an atmosphere of constant base-state wind and isothermal stratification, l is a constant and is given by:

$$l^2 = g^2 \left(\frac{1}{C_p \bar{T} \bar{U}^2} - \frac{1}{4 R^2 \bar{T}^2} \right). \tag{13.8.2}$$

Assuming that the disturbances vanish as $x \to \infty$, the bottom boundary condition is linearized $\delta(x,0) = h(x)$, and applying an upper radiation boundary condition, the solution for perturbation streamlines is of the form

$$\delta(x, z) = \left(\frac{\bar{\rho}}{\rho_o} \right)^{-\frac{1}{2}} h_m a \, \frac{a \cos(lz) - x \sin(lz)}{x^2 + a^2} . \tag{13.8.3}$$

where ρ_0 is the air density at z=0, h_m and a are, respectively, the mountain height and half-width of a bell-shaped mountain defined by

$$h(x) = \frac{h_m a^2}{x^2 + a^2} . \tag{13.8.4}$$

The velocity fields are calculated from the perturbation streamlines, so that

$$w'(x,z) = \bar{U} \frac{\partial \delta(x,z)}{\partial x} \tag{13.8.5}$$

and

$$u'(x, z) = -\frac{\bar{U}\partial(\rho\delta(x, z))}{\rho\partial z} \tag{13.8.6}$$

where *u'* is derived from *w'* using the anelastic continutity equation.

b) Numerical Results

ARPS is verified against the 2-dimensional exact solutions of the linear waves discussed earlier. For this test, the model flow was initialized over a period of 5 non-dimensional time ($\bar{U}$ t/*a*) units. This was done by linearly increasing the base state wind ($\bar{U}$) and total winds by the same amount until $\bar{U}$ reaches the desired value at $\bar{U}$ t/*a* = 5. The lateral boundary condition of Klemp-Lilly (1978) and Durran and Klemp (1983) discussed in Section 6.5 was applied at the lateral boundaries. In addition, a small amount of relaxation was applied at the inflow boundaries. Minimal horizontal computational mixing was used to remove grid scale noise. A Rayleigh damper was applied to the top half of the computational domain. The key parameters used by this and a finite-amplitude mountain wave experiments are summarized in Table 13.1. A more complete list can be found in file *mwav1a.input* located in *arps40.valiate* directory.

Table 13.1 ARPS mountain wave test parameter summary.

Parameter	Linear Mountain Wave	Non-linear/Non-Hydrostatic
Δx (m)	2000	400
Δz (m)	250	125
nx	99	363
nz	99	147
dtbig (s)	20	10
dtsml (s)	5	1
$\bar{U}$ (m/s)	20	10
$\bar{T}$ (Kelvin)	250	N = 0.01 s^{-1}
h_m (m)	1	500
a (m)	10000	2000
Rayleigh damping coef. (1/s)	0.0015	0.0025
height damper starts (m)	12000	9000
horizontal mixing (4th order)	6.0×10^{-5}	6.0×10^{-5}
vertical mixing	0	0

Figure 13.8 presents the fields for u', w', θ' and p' for the entire computational domain at $\bar{U}\,t/a$ = 60 or t = 30,000 s. Figure 13.9 compares ARPS predicted steady state u' and w' fields at t = 30000 s to the steady state analytic solutions in a 80 x 12 km^2 domain.

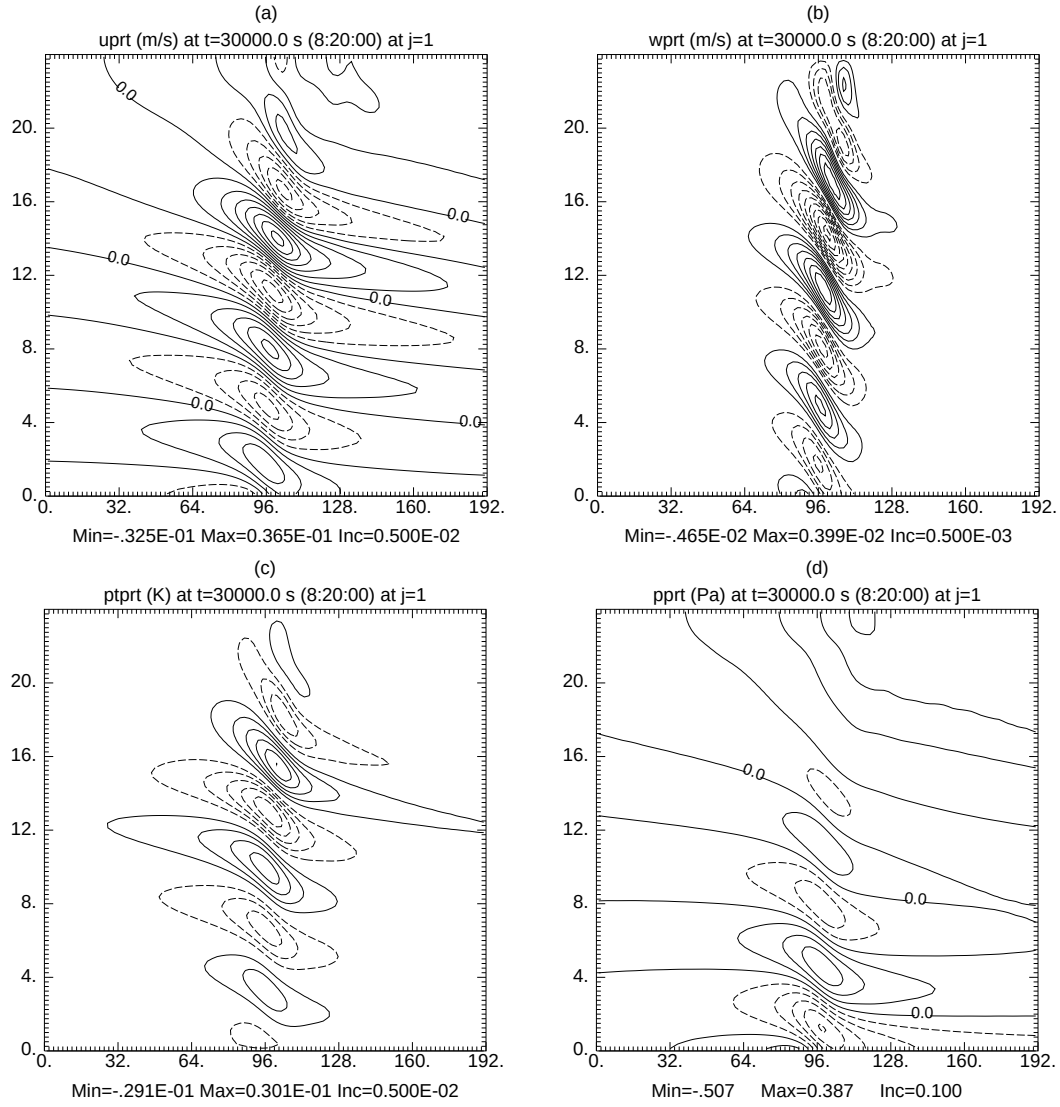

Figure 13.8. ARPS numerical solutions at time $\bar{U}t/a$ = 60 (t=30,000 s) for u' (a), w' (b), θ' (c), and p' (d) for linear hydrostatic mountain waves. Contour intervals are (a) 5×10^{-3} m s^{-1}, (b) 5×10^{-4} m s^{-1}, (c) 5×10^{-3} K, (d) 0.1 Pa.

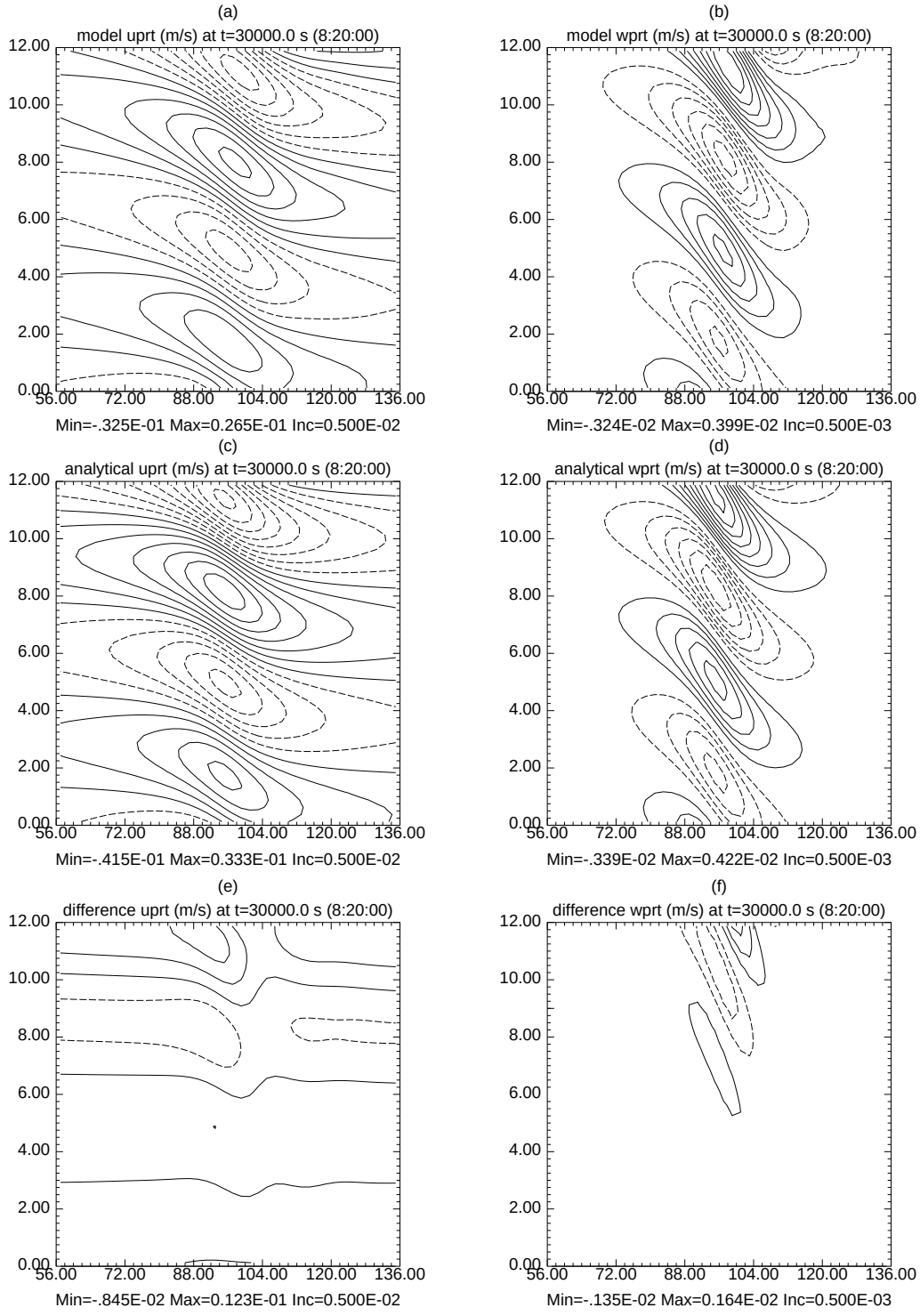

Figure 13.9. ARPS predicted u' (a), w' (b) at time $\bar{U}t/a = 60$ (t = 30,000 s), the steady state analytic solutions for u' (c) and w' (c), and the difference of u' (e) and w' (f) of ARPS prediction from the analytic solution, for linear mountain waves. Contours are (a) 0.005 m/s, (b) 0.0005 m/s, (c) 0.005 m/s, (d) 0.0005 m/s, (e) 0.0025 m/s, and (f) 0.00025 m/s. Area displayed is 80 km wide and 12 km deep.

The difference fields in Figs. 13.9(e) and (f) indicate errors in ARPS predicted fields that are on the order of 10-20 % near the top of the undamped layer. Errors near the ground are substantially smaller. Most of the error appears to be associated with the slight downstream tilt of these waves. In addition, the model maxima and minima are smaller in magnitude in comparison with the analytic solution with the differences increasing with height. This is consistent with results from Nance and Durran (1994) for a compressible model. Their study compared a compressible model to a number of anelastic models and showed errors in their compressible model that are similar to those of ARPS shown in Figure 13.9.

c) Momentum Flux

Another important measure of the model performance is the vertical flux of horizontal momentum, which is defined as

$$M(z) = \int_{-\infty}^{+\infty} \bar{\rho} u' w' \, dx \,. \tag{13.8.7}$$

Eliassen and Palm (1960) showed that for linear steady-state hydrostatic mountain waves, the vertical flux of horizontal momentum is constant with height and is given by

$$M_h = -\frac{\pi}{4} \rho_o N \bar{U} h^2 \tag{13.8.8}$$

where ρ_0 is the surface reference density and N the static stability. For an isothermal atmosphere,

$$N = \frac{g^2}{C_p \bar{T}} \,. \tag{13.8.9}$$

The vertical fluxes of horizontal momentum are calculated for the ARPS solutions according to Eq. (13.8.7) and plotted in Figure 13.12 for three different model times ($\bar{U}\, t/a$ = 20, 40, 60). The plotted profiles are normalized by the analytic surface value given in Eq. (13.8.8). As the model solution approaches a steady state, the normalized momentum flux at heights below the damping layer should approach 1.0. Figure 13.10 shows the model predicted fluxes range between 0.92 and 0.97 from the surface to a height of one vertical wavelength (approximately 6.4 km) at non-dimensional time 60. Similar accuracy has been reported for other models by, *e.g.*, Durran and Klemp (1983), Xue and Thorpe (1991).

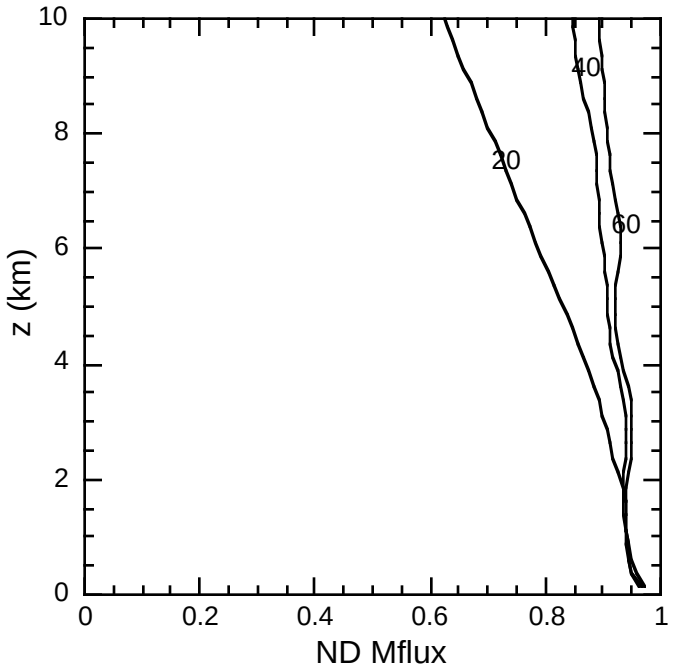

Figure 13.10. ARPS predicted normalized vertical momentum flux for a linear hydrostatic mountain wave. Curves 20, 40, and 60 represent normalized momentum fluxes at non-dimensional times of $\bar{U}\,t/a$ = 20, 40, and 60, respectively.

The accuracy of the low-level momentum fluxes are found to be sensitive to the low-level vertical resolution. A vertically stretched grid using a minimum Δz of 75 m at the surface and an average Δz of 250 m yielded a normalized flux value that is within 98% of the analytical values at the low levels. This result is consistent with the finding of Straka in his non-hydrostatic model (J. Straka, University of Oklahoma, personal communication). The normalized momentum fluxes using a stretched vertical grid are presented in Figure 13.11.

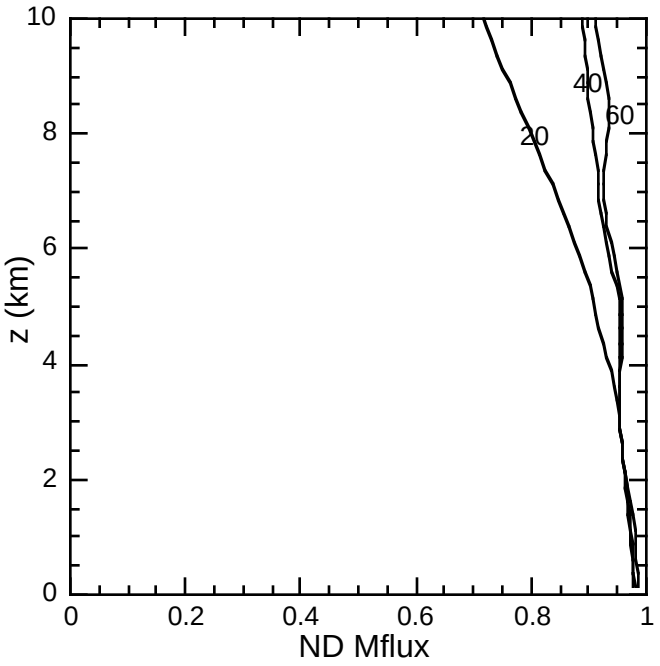

Figure 13.11. ARPS predicted normalized vertical momentum flux for a linear hydrostatic mountain waves using a stretched vertical grid with a minimum Δz of 75 m and an average Δz of 250 m. Curves labeled with 20, 40, and 60, represent normalized momentum flux at non-dimensional times of $\bar{U}\, t/a$ = 20, 40, and 60, respectively.

13.8.2. Finite Amplitude Non-Hydrostatic Non-Rotating Mountain Waves

a) Analytic Solution

An analytic solution to Long's equation (1953) is used to verify ARPS numerical solution. The non-hydrostatic non-linear 2-dimensional set of equations have an analytic solution under the constraints of the Boussinesq approximation. The governing equations for streamline displacement from the undisturbed upstream value is given by:

$$\frac{\partial^2 \delta}{\partial x^2} + \frac{\partial^2 \delta}{\partial z^2} + l^2 \delta = 0 \qquad (13.8.10)$$

where δ is the streamline displacement and l the Scorer parameter ($N/\bar{U}$). Assuming that the disturbances vanish as $x \to \infty$, the bottom boundary condition is linearized, and the upper radiation boundary condition is applied, the solution for streamline deflection is (Durran and Klemp, 1983):

$$\delta(x, z) = h_m a \,\mathrm{Re}\left[\int_0^l \exp\left(i\left(kx + \left(l^2 - k^2\right)^{1/2} z\right) - ka\right) dk + \int_l^\infty \exp\left(ikx - \left(k^2 - l^2\right)^{1/2} z - ka\right) dk\right], \tag{13.8.11}$$

where h_m is the mountain height and a is the mountain half-width. The mountain profile is given by Eq. (13.8.4). The above solution satisfies the linearized bottom boundary condition only. For a finite-amplitude mountain, the bottom boundary condition is non-linear. To enforce the non-linear condition,

$$\delta(x, z_s) = z_s , \tag{13.8.12}$$

Equation (13.8.11) is numerically integrated and iterated to satisfy the non-linear condition. The iterated terrain profile was then used to force the flow in ARPS. The iteration method follows the Steffensens Algorithm provided by Burden and Faires (1989). The initial mountain height was 570m and the mountain half-width was 2000 m. The final iterated mountain crest was approximately 500 m with the peak shifted a few hundred meters upstream.

In terms of streamline deflection, the analytically determined perturbation velocity fields are:

$$u_a(x, z) = -\bar{U}\frac{\partial \delta(x, z)}{\partial z} , \tag{13.8.13}$$

$$w_a(x, z) = \bar{U}\frac{\partial \delta(x, z)}{\partial x} . \tag{13.8.14}$$

The analytic velocity fields were computed using the same horizontal grid spacing as the model grid but with an increased vertical grid spacing of 41.67 m.

b) Numerical Results

The key parameters of the non-linear test are given in Table 13.1. A more complete list can be found in file *mwav4a.input* located in directory *arps40.valiate* of ARPS official release. The ARPS code was modified to enforce the Boussinesq approximation. This required the removal of the perturbation pressure buoyancy term in the vertical momentum equation and the pressure advection terms in the pressure equation. The modified pressure equation includes only the divergence term and the local time rate of change of pressure. The sound waves supported by the equation system should have

little effect on the steady-state gravity wave solution. To force the atmosphere to be Boussinesq, the base-state density takes on an average tropospheric value of 0.86 kg/m^3. Similar modifications were made to ARPS in Xu, *et al.* (1995) for the simulations of density currents. ARPS was run using the vertical implicit option with a big time step size of 5 seconds and a small time step size of 1 second.

As was done for the linear wave test, ARPS was initialized over a period of 5 non-dimensional time units in order to reduce the initial transient response. Other setups of the model are also similar to the linear wave test reported in the previous subsection. These include the application of the radiation condition at the lateral boundary, a very small amount of computational mixing (*cfcm4h* = 0.0006) in the horizontal, and a Rayleigh damping layer in the top half of the computational domain.

Trajectories were calculated from model-predicted winds using a predictor-corrector method and compared to the analytic solution. When the flow is steady, the trajectories become streamlines. The calculated streamlines start at 1 km vertical intervals at the inflow boundary. The time step used to compute the trajectories was 5 seconds, which is equivalent to a Courant number of 0.3. Figure 13.12 provides a comparison of the analytic streamlines (dashed) and ARPS-predicted streamlines (solid) at $\bar{U}t/a$ = 40 (8000s). At this time, the ARPS solution is nearly steady.

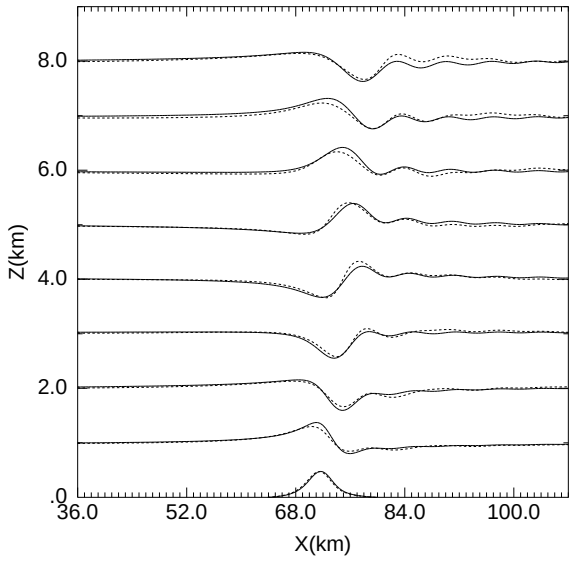

Figure 13.12. Comparison at time $\bar{U}t/a$ = 40 for analytic streamlines (dotted line) and ARPS numerically predicted streamlines (solid line). The upstream vertical streamline interval is 1 km.

In general, ARPS reproduces the analytic solution quite well. The noticeable differences are in the region directly over and downstream of the mountain. Errors in this test follow the patterns seen in the linear mountain wave test presented earlier - the model has a tendency to tilt the wave upstream with height. By comparison, the streamlines produced by Durran and Klemp (1983) are somewhat superior to the ARPS solution, although both models employ similar time and space differencing schemes. These differences are addressed below.

A more quantitative comparison of model and analytical velocity fields is made. In Figure 13.13, u' and w' from ARPS are plotted in a) and b), analytic u' and w' fields are given in c) and d), and the difference fields (model-analytic) are presented in e) and f), respectively. In general, the model and analytic u' and w' patterns are in good agreement in terms of the location and magnitude of the maximum and minimum values. However, the difference fields depict a secondary circulation above and downwind of the mountain. The circulation is largely non-divergent and is therefore not related to acoustic modes. The likely cause is the reflection of vertically propagating gravity waves off either the Rayleigh damping layer or the rigid model top boundary. A number of tests were conducted trying to improve the reflection characteristics of this test. The depth (up to 2 times the vertical wavelength), strength, and type of damping coefficient function (sine, cosine, linear, and tanh) were varied, but no significant improvement was achieved over the results presented here. The resulting reflected circulation is on the order of 10-20% of the forced wave solution. Klemp and Lilly (1978) performed a wave reflection analysis on a hydrostatic linearized set of equations, their results indicate that for optimal modeling conditions, reflection on the order of 2 to 5% is expected from the damping layer and/or the top of the model. It appears that the non-linear and non-hydrostatic effects contribute further to the reflection. Work is currently underway to implement and test the upper radiation boundary condition of Klemp and Durran (1983).

Momentum fluxes were computed for the non-linear non-hydrostatic mountain waves presented above. ARPS predicted momentum flux at levels above the mountain are plotted in Figure 13.14. The flux was computed according to Eq. (13.8.7) and was normalized by the corresponding analytic value. Worth noting is that the integral in Eq. (13.8.7) is evaluated at constant height levels, after u' and w' were interpolated from the terrain-following model grid to constant height levels. The normalized fluxes are plotted at non-dimensional times ($\bar{U}t/a$) 20, 40, 60, and 80 in Figure 13.14. For a steady-state non-linear non-hydrostatic irrotating flow, the momentum flux should be constant with height. Figure 13.14 shows the model predicted fluxes are between 0.97 and 1.02 from the surface up to one vertical wavelength (approximately 6.4 km) height at $\bar{U}t/a = 80$. This accuracy is comparable to other published results.

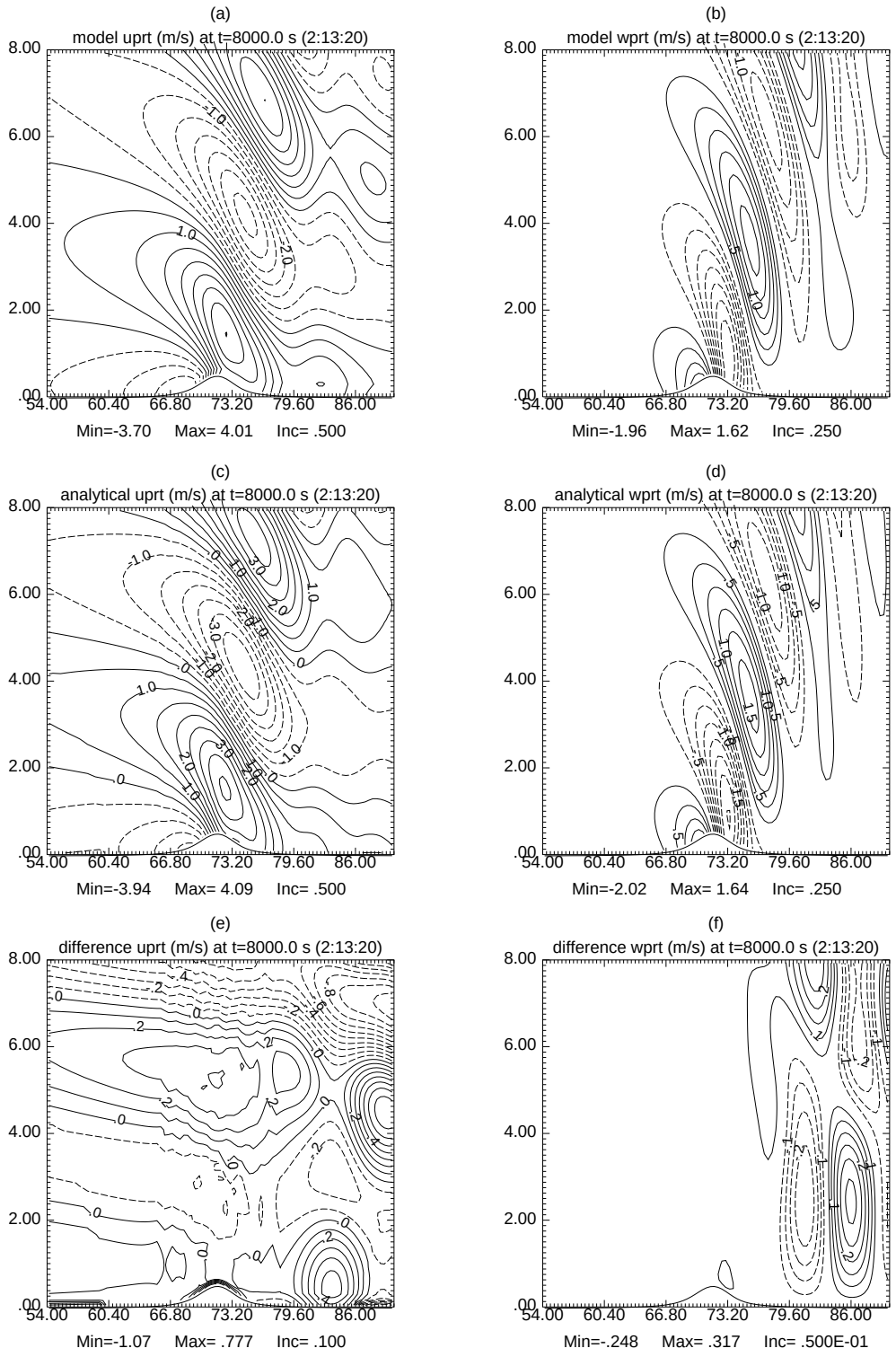

Figure 13.13. ARPS solutions at time $\bar{U}t/a = 40$ (8,000 sec) for u' (a) and w' (b), the steady-state analytic solutions for u' (c) and w' (d), and the difference fields (model-analytic) for u' (e), and w' (f) for Long's solution. Contour intervals are (a) 0.5m/s, (b) 0.25m/s, (c) 0.5 m/s, (d) 0.25 m/s, (e) 0.10 m/s and (f) 0.10 m/s. Only a subdomain 32 km wide and 8 km deep is displayed.

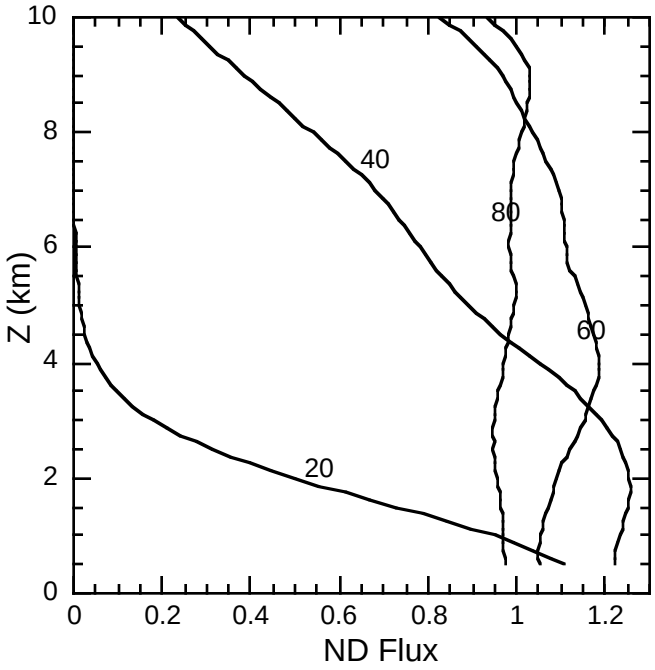

Figure 13.14. ARPS predicted normalized vertical momentum flux for non-linear non-hydrostatic non-rotating Boussinesq mountain waves at non-dimensional times $\bar{U}t/a$ = 20, 40, 60, and 80.

13.8.3. Additional Notes on the Lateral Boundary Conditions

In the process of testing ARPS for linear and non-linear mountain flows, a number of items were noted regarding the limitations of the lateral boundary conditions. During the linear tests, the vertically averaged phase speed option (*rbcopt* = 4) was found to be superior to the other types of lateral boundary condition. This was especially evident in the perturbation pressure field. It was noted that, even with an one meter high mountain. Weak gravity waves incident on the lateral boundary produced a pressure drift on the order of magnitude of the forced mountain wave perturbation pressure field when the open boundary option two was used. The vertically averaged phase speed option reduced the pressure drift to approximately 20% of the expected perturbation value. The pressure detrending option available in ARPS is very effective in removing the pressure drift, but was not employed in the tests shown here.

The effect of lateral boundary conditions on strongly forced flows is more pronounced. In the finite amplitude Long's solution tests, the streamlines computed using a smaller domain (183×75) were affected by a nearly domain-wide pressure drift. Durran and Klemp (1983) noted in the Long's solution test of their model, the downstream streamlines were not

recovering to the upstream values. This phenomenon was also observed in the ARPS solution. Tests were conducted with varying lateral domain sizes. This error was largely eliminated when the domain size is doubled; also, the pressure field exhibited a smaller, though still noticeable, drift. Interestingly, the pressure drift disappeared when periodic conditions were applied at the lateral boundaries, suggesting that the boundary conditions were the cause of the problem. Therefore, care must be given to the treatment of lateral boundaries when the model is run for a long period of time. Improvements to the lateral boundary conditions are being investigated.

13.9. 1-D Benchmark Tests on Soil Model

Two benchmark runs have been made to test ARPS soil model with the Wangara and FIFE databases. A 1-D domain was chosen with 101 vertical levels (*nz* = 103) and an interval of 100 m. Physical processes including microphysics and Smagorinsky/Lilly subgrid scale turbulence were activated. The stability-dependent surface flux option was chosen.

The soil and vegetation property parameters and initial conditions for soil variables for the Wangara and FIFE cases are listed in the following table (Table 13.2).

Table 13.2. Soil and vegetation parameters and initial values for soil variables

Parameter	Wangara	FIFE
Soil Type	Loam	Silty clay loam
Veg. Type	Dessert	Grassland
Roughness	0.24	6.5
LAI	0.1	2.8
Veg. (%)	5	99
T_s	275.69	295
T_2	276	297
W_g	0.1533	0.270
W_2	0.1550	0.255
W_r	0.000	0.000

For the Wangara case, the sounding (*wangara.snd*) is dry. The potential temperature increases linear from 278° K to 304° K within a 4 km depth. The sounding for the FIFE case was taken from an actual observation at site grid number 0928 at 12:00Z, July 11, 1987 (*fife_july11.snd*). The input

and sounding files for these two cases are included in ARPS distribution package, and are located in directory *arps40.validation/soil.validate*.

13.9.1. Wangara case

This case is a 48-hour simulation of days 33 and 34 of the Wangara Boundary Layer Experiment (16 and 17 August 1967, Clarke *et al*., 1971). These two particular days are used quite often as test cases for PBL and heat flux algorithms. In general, the modeled fluxes compare very well with the observations. The agreement of the observed and simulated net radiation indicates that simple radiation model is sufficient for such dry environment.

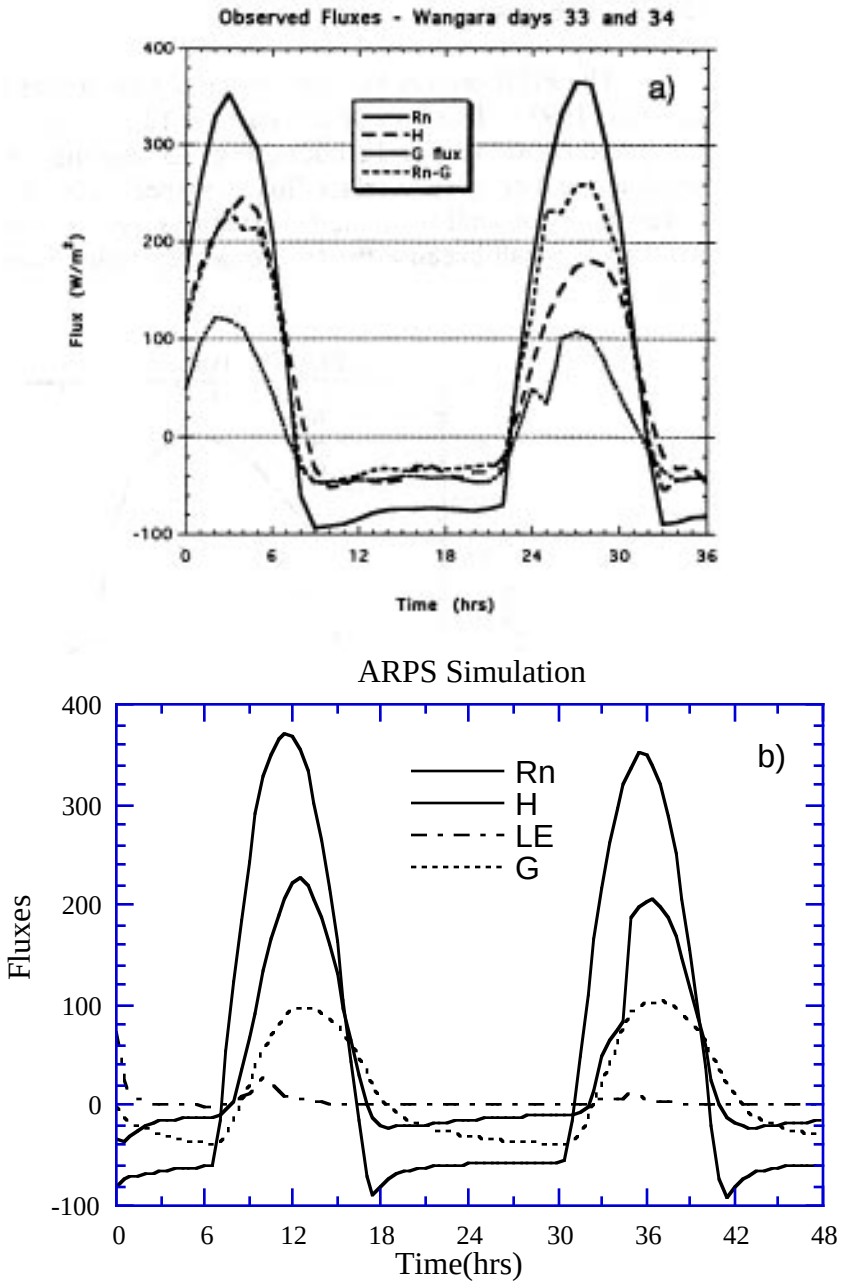

Figure 13.15 A comparison of the observed and simulated surface fluxes of net radiation (Rn), sensible heat (H), latent heat (LE), and ground heat (G) for Wangara days 33 and 34. Hour 0 is 0900 LT in the observation plot while hour 0 is 0100 LT in the simulation plot.

13.9.2. FIFE case

The FIFE project has been described by Sellers *et al.* (1992) and Pleim and Xiu (1995). This simulation starts at 12:00 UTC (7:00 CDT), on 11 July 1987, and continues for 12 hours. Fig. 13.16a and 13.16b show the model-simulated and observed surface fluxes, respectively. In general, the simulated fluxes compare well with the observations. Note that the simulated ground heat flux is small because the fractional vegetation coverage is assumed to be 99%.

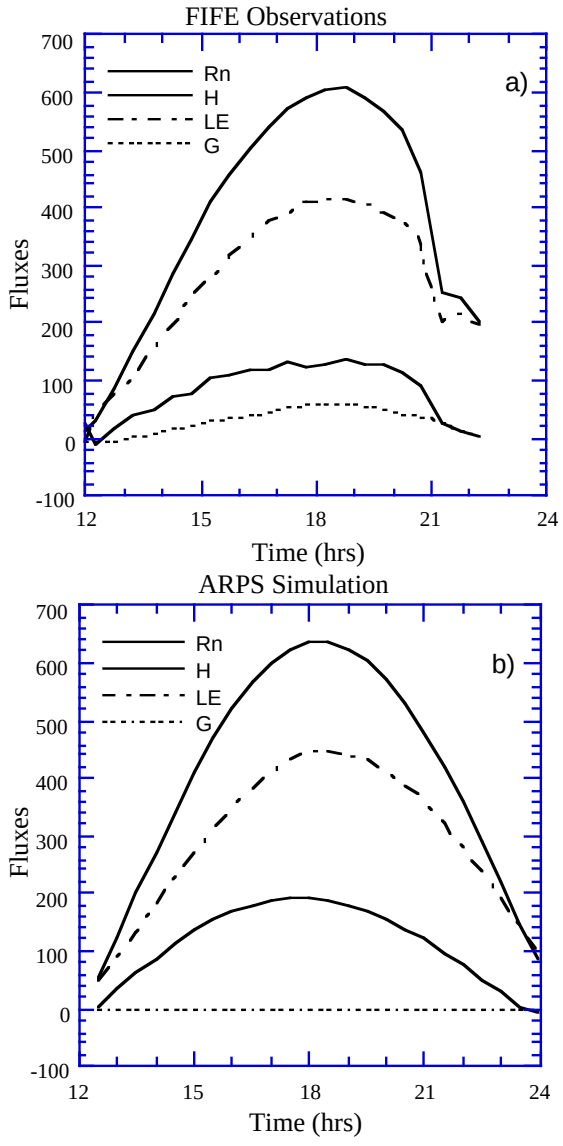

Figure 13.16 A comparison of the observed and simulated surface fluxes of net radiation (Rn), sensible heat (H), latent heat (LE), and ground heat (G) for 11 July 1987 of FIFE. UTC time has been used.

13.10. A Real Data Example

During spring 1995, CAPS conducted a daily real-time prediction experiment with ARPS, in collaboration with the VORTEX '95 field experiment (Rasmussen, *et al.*, 1994) . This experiment represents the first time that a numerical model initialized with non-homogeneous initial and boundary conditions is used for real-time storm-scale weather prediction (Xue *et al.*, 1995).

To summarize, two 6-hour forecasts were made each day. One is on a 1200x1200 km domain centered over western Oklahoma, with 15 km resolution. Initial and boundary conditions were taken from the forecasts of Rapid Update Cycle valid at 18Z, 21Z and 00Z. This set of forecasts used a vertically stretched grid, 1.5 order TKE turbulence, Kuo cumulus parameterization and stability-dependent surface flux formulations coupled with a soil model that predicts the soil surface temperature and moisture. Each 6-hour forecast took about 20 minutes wall-clock time on 2 dedicated processors of a Cray C90. The second set of forecasts used a 3 km resolution grid over a 336 x 336 km domain. The location of this grid is targeted at the prime area of severe weather each day, as determined by VORTEX forecasters and examiniation of the 15 km ARPS prediction. This domain is one-way nested within the 15 km resolution domain described above, using the same physics except with Kessler microphysics instead of the Kuo cumulus parameterization. Initial data for this run was from the OLAPS analysis (Brewster *et al.*, 1994). The 6 hour forecast took about 45 minutes of wall-clock time on a 256 node partition of a Cray T-3D.

One 3 km resolution forecast is presented here as an example. Between 18Z and 20Z, June 8, 1995, a cluster of storms occurred in the Texas and Oklahoma panhandle area at a triple point between an E-W oriented surface front and a N-S oriented dryline . By 00Z, June 9, the storms organized into a SW-NE orientation (see Figure 13.17a), and the storm at the southern end spawned destructive tornadoes. ARPS successfully predicted this cluster of storms a few hours in advance on the 3 km grid (Figure 13.17b).

The daily forecasts were made available in real time during that period and are accessible on the CAPS WWW page at *http://wwwcaps.uoknor.edu.* With the ARPS source code release, data for a reduced-domain test case using a 3-D initial data set and externally forced boundary conditions will be provided as an example.

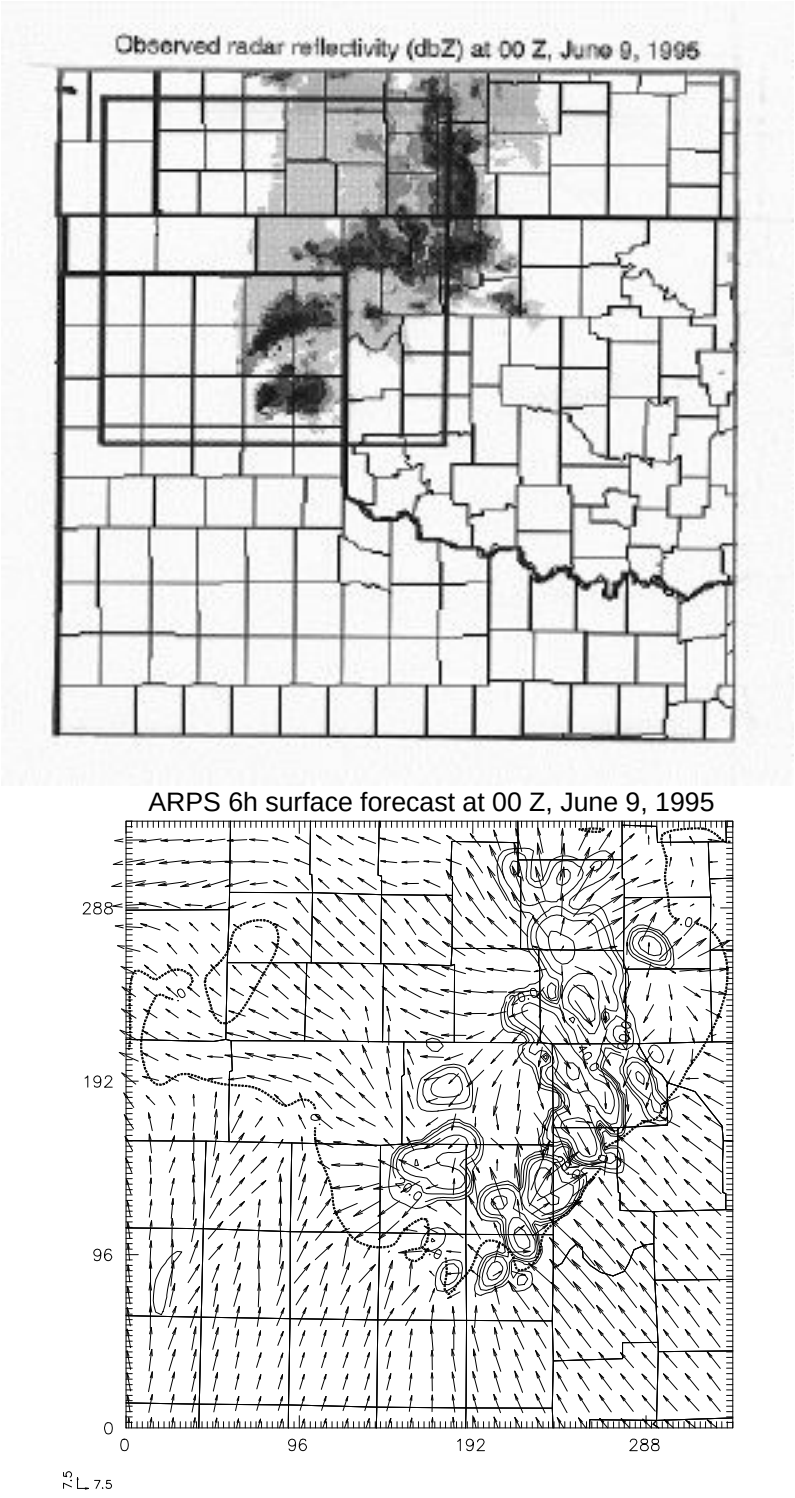

Figure 13.17. Observed (a) and predicted (b, in contours) low-level radar reflectivity fields at 00Z, June 9, 1995. Panel (b) also includes the predicted surface winds and a zero θ' contour shown in thick lines. The squared box in panel (a) corresponds to the forecast domain in panel (b).